nature communications

Article

https://doi.org/10.1038/s41467-024-54904-9

# Designing $Ni_2MnSn$ Heusler magnetic nanoprecipitate in copper alloy for increased strength and electromagnetic shielding

Received: 22 May 2024

Accepted: 20 November 2024

Published online: 03 December 2024

Check for updates

Zhuoran Xia[1], Xiangyi Huang[1], Jiaqi Liu[1], Wen Dai[1], Liuxiong Luo[1], Zhaohan Jiang[1], Shen Gong[1,2] ✉, Yuyuan Zhao[3,4] & Zhou Li[1,2] ✉

Structural electromagnetic shielding materials are required to withstand high stress and electromagnetic interference in extreme environments. In this paper, a nano-magnetic Heusler phase with desired structure parameters was successfully obtained in a copper matrix by employing a multi-objective driving design strategy. The resulting copper alloy exhibits a yield strength of up to 1.5 GPa, and the attenuation degree of electromagnetic wave reaches 99.999999999% (110 dB) within the frequency range of 10 kHz to 3 GHz. The research suggests that the $Ni_2MnSn$ precipitates with optimized structure parameters (including high number density: $5 \times 10^{23}\,m^{-3}$, small size: 23 nm, large aspect ratio: 4, low mismatch: 2.3%, strong bonding: -0.316 eV/atom, magnetic order: 4.05 $\mu_B$/f.u.) both reinforce the matrix by strong pinning and enhance electromagnetic shielding properties through magnetic-electric coupling. This design method tailored for multiple performance requirements provides a valuable tool for the development of structure-function integrated materials.

Electromagnetic shielding materials (EMSMs) with integrated structure-functionality have been widely employed[1,2], such as in base station enclosures[3]. With expanding application scenarios of 5 G communication[4], military electronic devices, and satellite technologies[5], there is a growing demand for EMSMs that can withstand greater stresses while retaining strong electromagnetic shielding capability. Currently, the design of EMSMs[6–8] often relies on the formation of composites to achieve multiple functionalities. However, substantial hurdles are encountered to achieve ultra-high strength (yield strength > 1000 MPa) and ultra-high electromagnetic interference shielding effectiveness (EMI-SE > 100 dB within the GHz frequency range). On one hand, there is insufficient effort to achieve high mechanical strength by combining multiple strengthening features. This, in many instances, is attributable to inherent low strength of the substrate material[9,10] or weak interfacial bonding[11] and stress transfer[12] among different constituents. On the other hand, the dispersion effect intrinsically reduces the crucial electromagnetic parameters of materials (such as permeability and dielectric constant) during the propagation of electromagnetic waves, resulting in lower loss capability at high frequencies.

The size and geometry of ferromagnetic materials are two key factors for enhancing shielding effectiveness at high frequencies. Nano-scale magnetic materials boast a higher specific surface area than their micron-scale counterparts, and therefore enhance interactions with microwaves. By incorporating shape anisotropy, the shielding effect at high frequencies can be further enhanced[13] due to the increase in resonance frequency[14]. Therefore, the current microstructure-design approaches for electromagnetic shielding tend to obtain magnetic materials with smaller sizes and larger aspect ratios[15,16]. Moreover, the dislocation bowing strengthening mechanism shows that higher degrees of dispersion of particles, i.e., smaller particle sizes (1–100 nm)[17] result in greater increases in internal stress.

[1]School of Materials Science & Engineering, Central South University, Changsha 410083, China. [2]State Key Laboratory of Powder Metallurgy, Changsha 410083, China. [3]School of Engineering, University of Liverpool, Brownlow Hill, Liverpool L69 3GH, UK. [4]School of Mechanical and Automotive Engineering, Ningbo University of Technology, Ningbo, China. ✉e-mail: gongshen011@csu.edu.cn; lizhou6931@csu.edu.cn

Hence, it is crucial to design particles with improved structural parameters, including high number density, small size, large aspect ratio, magnetic order, etc., to realize a combined improvement of strength and electromagnetic interference shielding effectiveness (EMI-SE).

NiMn-based Heusler compounds have attracted extensive research interest[18–20] due to their unique magnetic properties and highly symmetrical ordered $L2_1$ structures. In electromagnetic shielding applications, they exhibit multi-resonance characteristics[21,22] in magnetic loss factor and significant dielectric relaxation[21]. However, their severe grain boundary brittleness has hindered their applications[23].

To overcome the brittleness problem of the NiMn-based Heusler compounds, we here introduce the constituent elements of the Heusler phase into a conductive Cu metal matrix and trigger the formation of magnetic precipitates with high aspect ratios through aging treatment. Previously, Heusler compounds were usually acted as mechanically strengthened phases when added to metals or solid solutions. Jang et al.[24] designed shear band-driven Co-rich Heusler precipitate in the middle entropy alloy to achieve ultra-high strength and ductility. J. Milla´n[25] and Kim[26] obtained the dispersion distribution of coherent ordered Heusler phase in Fe matrix and high entropy matrix, respectively, through the minimum lattice mismatch, resulting in high cutting stress. However, we hope that the designed Heusler compounds can meet multiple objectives at the same time. Han et al.[27,28] formulated different phase design constraint rules for target properties, realized various phase structure characteristics, and obtained multi-element alloys with different advantages. Inspired by this idea, a synergistic enhancement of mechanical strength and EMI-SE is achieved by controlling the structure parameters of the Heusler phase.

We propose four rules to be followed in optimizing the structure parameters: (1) The uniformity of the microstructure and the phase stability are required. Therefore, the constituent elements of the Heusler phase have some solubility in the matrix while having a relatively negative formation energy, to enable the formation of a supersaturated solid solution and subsequent precipitation under suitable conditions; (2) Lattice mismatch is low, to reduce the formation barrier[29,30], inhibit competitive coarsening[27], and form a continuous lattice to improve interfacial adhesion; (3) The growth of particles in the matrix has one or two directions of minimal elastic mismatch while having significantly higher elastic strain energy in other growth directions, to obtain shape anisotropy morphology features; (4) The phase structure possesses a high effective magnetic moment, to enhance the capacity for magnetic loss.

In this paper, density functional theory calculations and data-driven screening were employed to identify the $Ni_2MnX$ phase, thus obtaining the optimal alloy composition[31]. Among the eight elements (X) capable of forming Heusler compounds, Sn was identified as preferable to the other elements, as the $Ni_2MnSn$ phase was found to satisfy the requirements of structure parameters. A series of Cu-Ni-Mn-Sn alloys with ultra-high strength and high EMI-SE were prepared. Well-controlled particle size distribution was obtained through composition-process design, ensuring an optimized combination of high strength, magnetism, and electrical conductivity. The characteristics of the structure parameters of the $Ni_2MnSn$ phase and their impact on strength and EMI-SE were analyzed using techniques such as atom probe tomography (APT) and high-angle annular dark-field (HAADF) imaging. The Maxwell-Garnett theory[32], multi-scale transmission matrix models[33,34] and classical mechanical calculations were used to elucidate the synergistic enhancement of strength and EMI-SE via the nano-scale anisotropic magnetic phase.

## Results

### Data-driven phase screening

The first step of our structure parameters design strategy involves data-driven phase screening to effectively design magnetic $Ni_2MnX$ Heusler phase in Cu matrix. Figure 1 illustrates a multi-objective screening scheme for X elements based on density functional theory calculations. We selected Ga, Sn, In, Sb, Al, Ge, Zn, and Si as the candidates according to the color scheme for Heusler compounds

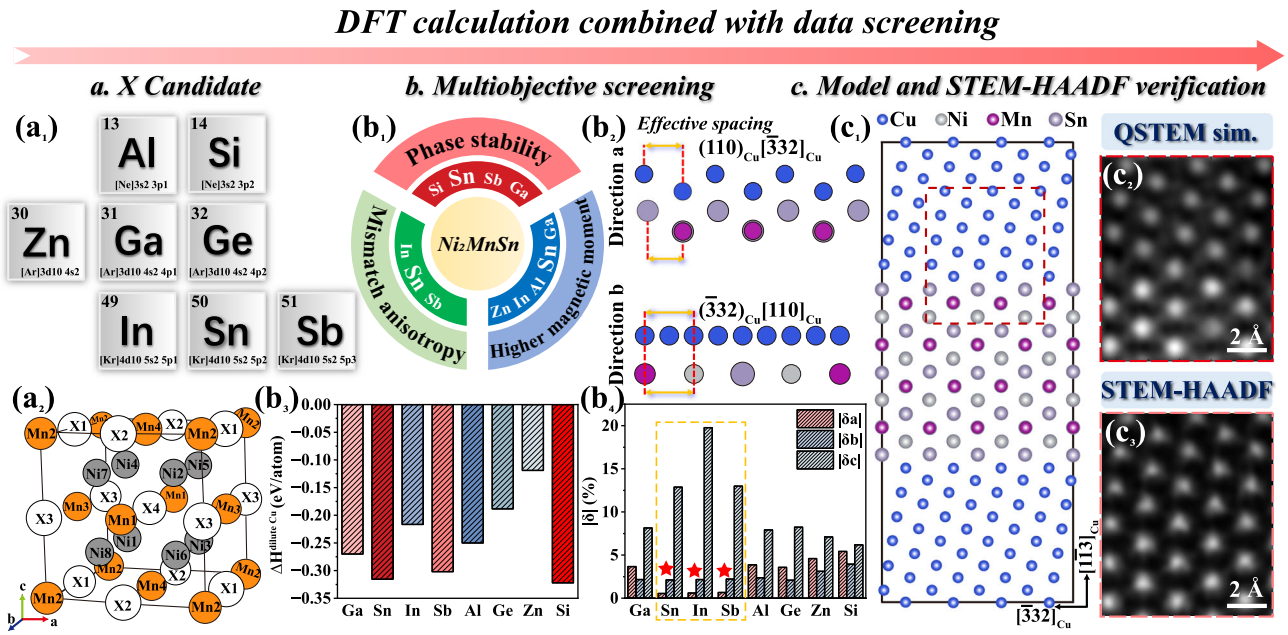


**Fig. 1 | Framework for designing the $Ni_2MnX$ phase in the Cu matrix. a1** Candidates for X elements showing the electron configurations and (**a2**) the crystal structure of $Ni_2MnX$ phase. **b1** Depiction of the multi-objective screening scheme based on phase stability, anisotropic mismatch and high magnetic moment (see Supplementary Table 1 for results on magnetic moment) and (**b2**) schematic representations of the edge-to-edge[41] model showing matching atoms for sawtooth and linear rows. **b3** Formation energy of $Ni_2MnX$ candidates, where the red series of bars indicate relatively negative formation energy. **b4** The calculated effective atomic spacing of $Ni_2MnX$ candidates along the a, b and c axes, where the stars indicate strong anisotropy. **c1** Construction of a Cu-$Ni_2MnSn$-Cu sandwich interface model (X=Sn) and (**c2, c3**) verification of the HAADF results by QSTEM[44] atomic image simulations. Source data are provided as a Source Data file.

provided by Tanja Graf [35]. The solid solubility limits of these elements (including Ni and Mn) in Cu matrix are all greater than 5 at %. Phase screening was based on the aforementioned structure parameters design rules and was conducted by theoretical calculations in the following steps.

Density functional theory calculations were performed to obtain the enthalpy of formation of the $L2_1$-ordered $Ni_2MnX$ phase by considering $E_X^{\text{dilute Cu}}$ [25], i.e., the chemical potential of X in the Cu solid solution (Fig. 1b$_3$). The $L2_1$ compounds formed by the metallicity-weak elements Si, Sb, and Sn were found to be more stable. The relatively large electronegativity differences between each of these three elements and the Mn elements lead to considerable energy differences between bonding and antibonding d states, and therefore their strong bonding. Among them, the chemical potentials (Supplementary Table 2) of Sb and Sn in the Cu matrix (−3.53 eV/atom and −3.62 eV/atom, respectively) are more positive compared to those in free space (−4.01 eV/atom and −4.05 eV/atom, respectively), indicating a greater tendency for them to depart from the Cu matrix. In addition, the small mixing enthalpy(−15 kJ/mol-5 kJ/mol[36–38]) of atomic pairs formed by Sb, Sn, and Ni, Mn (Sn-Ni with a $\Delta H^{mix}$ of −4 kJ/mol, Sn-Mn with a $\Delta H^{mix}$ of −7 kJ/mol, Sb-Ni with a $\Delta H^{mix}$ of 1 kJ/mol, and Sb-Mn with a $\Delta H^{mix}$ of −11 kJ/mol) is more favorable in clustering and crystallization (Supplementary Table 3). (See Methods for detailed computational procedures.)

Subsequently, the calculated lattice constant of FCC-$L2_1$ was taken as an input parameter to the modified Bramfitt formula[39] to investigate the d-value mismatch of the close-packed plane (as detailed in the Methods and Supplementary Table 4). The only case where the formation of a continuous lattice with Cu occurs was determined, i.e., FCC {111} /$L2_1${220}. Under this condition, most elements were found to exhibit low mismatch values in the range of 2–2.3%, except for Si (3.9%). The relatively small lattice mismatch (less than 5%) is in conformity with the empirical law[40] of forming coherent interfaces.

In the next step, the edge-to-edge model[41] was used to compute the elastic mismatch anisotropy (as described in Methods). The $Ni_2MnX$ phases (X=Sn, In and Sb) exhibit similar and significantly elastic strain inhomogeneity (see Fig. 1b4). Sn, In and Sb are therefore crystallographically effective to form nanoparticles with a large aspect ratio on the low-energy crystal plane because of the low mismatch and elastic inhomogeneity with the Cu matrix. They were selected for further considerations.

It is noteworthy to point out that X elements themselves contribute minimally to the total magnetic moment. However, they can indirectly influence the oscillation of Mn atoms' RKKY interaction coupling[42,43] by altering the Mn-Mn distances at the third-nearest neighbor positions and affect the magnetic order. Collinear spin polarization calculations (Supplementary Table 1) revealed that the effective magnetic moment is relatively large (> 4 $\mu_B$/f.u.) where X = Zn, In, Al, Sn, and Ga. Considering all the screening criteria mentioned above, Sn was selected as the alloying element to form the Heusler phase $Ni_2MnSn$, which possesses the advantages of phase stability, high magnetic moment, low mismatch, and high elastic mismatch anisotropy.

Three Cu-Ni-Mn-Sn alloys, namely Cu-5.39Ni-2.94Mn-2.71Sn (wt%, designated as CA1), Cu-9.85Ni-6.02Mn-5.05Sn (CA2) and Cu-14.8Ni-9Mn-7.3Sn (CA3), were designed and assessed. CA2 was chosen as the main research focus. It was cast via vacuum induction melting and was subjected to conventional homogenization and thermomechanical treatment (Supplementary Fig. 1 and Methods). The aim was to obtain finely-dispersed, high-density magnetic $Ni_2MnSn$ particles through a rational combination of composition design and process design. Three possible interface terminations in the Cu-$Ni_2MnSn$-Cu sandwich model were considered and the most stable interface was obtained through structural relaxation calculations (see Supplementary Fig. 2 for specific calculation steps). Figure 1c shows that the relaxed structure along the Cu [110] zone axis simulated using the QSTEM[44] software is consistent with the actual HAADF result.

## Microstructure and precipitation behavior

The microstructure of the CA2 sample after thermomechanical treatment, finally aged at 300 °C for 128 h (Supplementary Fig. 1), was observed at the nanoscale. Figure 2a shows the nanoprecipitates with well-controlled particle sizes and a homogeneous distribution. The statistical results show a size distribution ranging from 5 to 60 nm, with an average diameter of 23 nm (see Supplementary Fig. 3 for detailed method and results). Locally magnified dark-field microscopic observations show distinctively oriented Widmanstätten nanopatterns[28] after aging (Fig. 2b, the principal orientations are indicated by arrows in different colors). The nano-precipitates exhibit a predominantly plate-like morphology, with an aspect ratio of approximately 4:1. The corresponding TEM energy dispersive spectroscopy (EDS) analysis (Fig. 2c1-c4 and Supplementary Fig. 4) and secondary diffraction peaks from XRD (Supplementary Fig. 5) confirm that Ni, Mn and Sn have strong chemical affinity and tend to form an ordered phase with an $L2_1$ structure.

The composition and 3D structure of the $Ni_2MnSn$ phase was analyzed quantitatively by atom probe tomography (APT) techniques. Fig. 2d1-d5 show that elements Ni, Mn, and Sn are primarily located in the $L2_1$ precipitates with Sn clearly defining the phase-matrix interface. The compositions of precipitated phase and matrix are accurately calibrated through the decomposition of peaks in marked regions of interest (Supplementary Fig. 6). The variation tendency of composition from the matrix to the precipitates is depicted by the 1D concentration profiles (Fig. 2e). Figure 2f provides 3D reconstructions of 3 at% Sn and 88 at% Cu iso-concentration surfaces, revealing the $L2_1$ and FCC phases, respectively. It shows that the interconnected, disordered FCC matrix serves as a framework and is filled with the ordered $L2_1$ phase. APT statistical measurements indicate a number density of $L2_1$ precipitates of approximately ~$5 \times 10^{23}$ m$^{-3}$. Observations from multiple angles of the APT tip (Fig. 2f) reveal that most precipitates have an anisotropic morphology (see Supplementary Movie 1). Figure 2h presents 2D contour plot of elements Cu, Ni, Mn and Sn, which correspond to the $L2_1$-FCC-$L2_1$ region in Fig. 2g, with pink indicating the highest frequency of enrichment. The distributions show non-abrupt changes in the concentrations of Cu, Ni, Mn and Sn from the interface towards the center suggesting the presence of a diffusion interface between the $L2_1$ phase and the Cu matrix.

The TEM and APT results collectively demonstrate the formation of $Ni_2MnSn$ precipitates with excellent structure parameters, including small size (23 nm), high number density ( ~$5 \times 10^{23}$ m$^{-3}$) and large aspect ratio (4:1). These results confirm the success and underscore the importance of the data-driven phase screening, guided by explicit objectives of ultra-high strength and high EMI-SE.

The spatial configuration of the steady-state $Ni_2MnSn$ phase in the Cu matrix were further investigated at the atomic scale. We employed high-angle annular dark-field (HAADF) scanning transmission electron microscopy (STEM) to capture the structures of the $Ni_2MnSn$ phase and the interface in the over-aged CA2. Figure 3a and f show the observations along the $[110]_{Cu}$// $[111]_{Ni2MnSn}$ and $[\bar{3}32]_{Cu}$// $[\bar{1}10]_{Ni2MnSn}$ axes. The atomic structures of the well-matched habit planes can be clearly seen at the locally magnified images (Fig. 3b, g). The Fast Fourier Transform (FFT) patterns (Fig. 3c, f) show that the two phases have clear crystallographic and interfacial orientation relationship, $(1\bar{1}1)$ $[110]_{Cu}$// $(\bar{2}20)$ $[111]_{Ni2MnSn}$ and $(1\bar{1}3)$ $[\bar{3}32]_{Cu}$// $(11\bar{2})$ $[\bar{1}10]_{Ni2MnSn}$, respectively. Fig. 3d1-d4 and Fig. 3i show the atomic column compositions obtained by atomic-resolution energy-dispersive X-ray spectroscopy (EDX). Overlap of Ni, Mn and Sn in the precipitate (Fig. 3d1-d4) and ordered arrangement of Sn atoms (Fig. 3i) can be observed. Figure 3j shows the atomic intensity profiles extracted from the transparent pink area in Fig. 3g. Combining Fig. 3d1-d4, 3i and j

https://doi.org/10.1038/s41467-024-54904-9

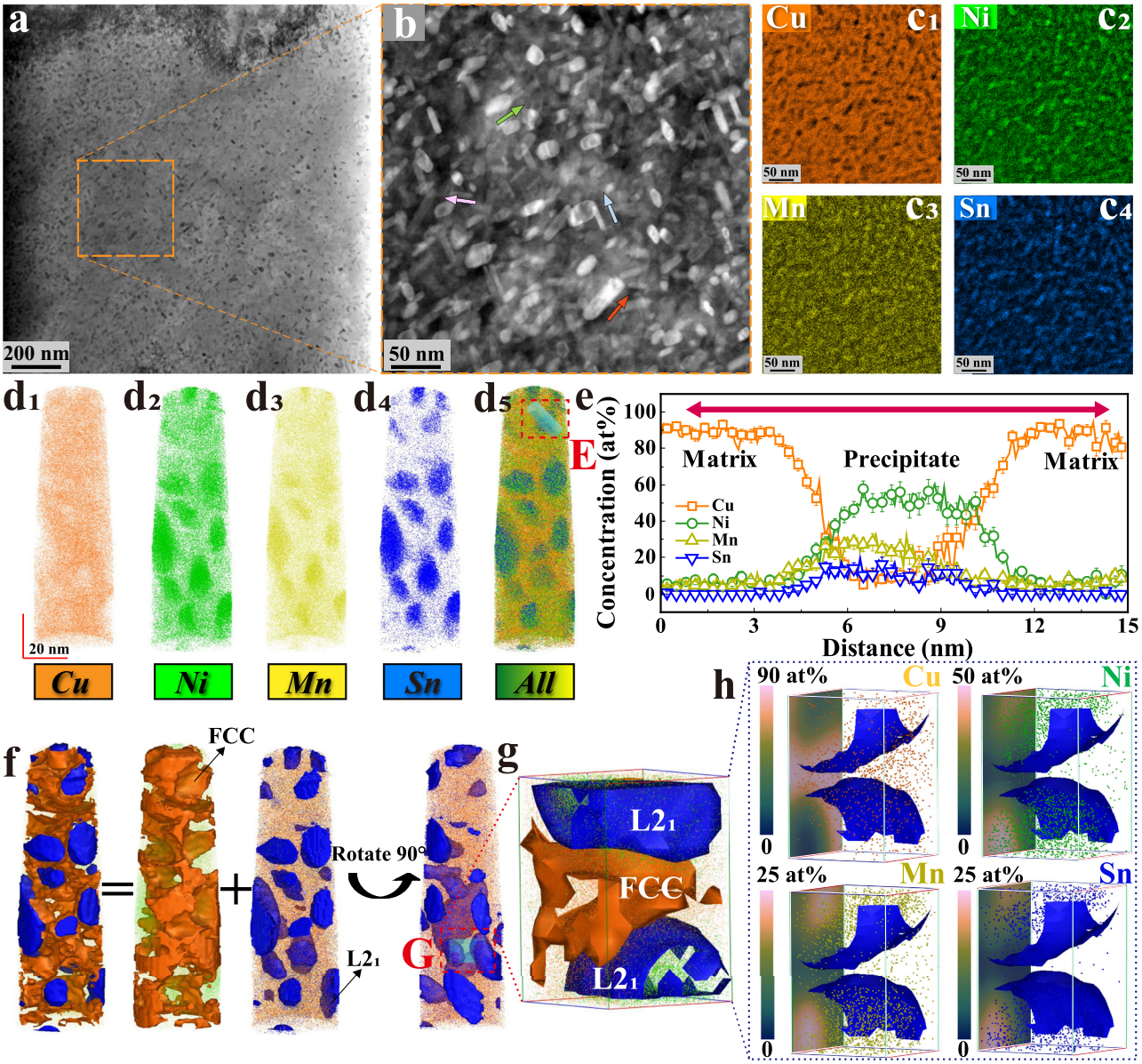


**Fig. 2 | Morphology of the $Ni_2MnSn$ phase in the Cu matrix. a** Representative bright-field image of the Cu-Ni-Mn-Sn alloy (CA2) displaying the distribution of nanoprecipitates. **b** Locally magnified dark-field image, with colored arrows showing different orientations of the particles. **c1-c4** TEM energy-dispersive spectroscopy (EDS) maps from (**b**). **d1-d5** APT reconstructed compositions of the FCC/$L2_1$ phase, where E indicate regions selected for further analysis. **e** 1D concentration profiles showing compositional changes across the FCC/$L2_1$/FCC interface, where error bars indicate a standard deviation. **f** 3D reconstruction of the morphology of the matrix and the nanoprecipitates via iso-concentration surfaces of Cu (88 at%) and Sn (3 at%), where G indicate regions selected for further analysis. **g** A box containing an $L2_1$-FCC-$L2_1$ structure (8 nm × 8 nm × 12 nm). **h** Corresponding atomic distributions and 2D contour plot (identical region with (**g**)). Source data are provided as a Source Data file.

reveals the ordered characteristic of the $L2_1$ phase where the heavier Sn-rich columns are interspersed with lighter Mn-rich (yellow spheres) and Ni-rich (green spheres) columns.

We found that the $Ni_2MnSn$ phases precipitate along the elastically soft Cu<100> direction in the early aging period by comparing selected area electron diffraction (SAED) patterns (Supplementary Fig. 7) at different aging stages. Lattice distortion and rigid rotation will occur in the subsequent aging process. The $Ni_2MnSn$ phase exhibits a typical Kurdjumov-Sachs (K-S) orientation relationship with the matrix (Fig. 3c) in the steady state, where the closest packing planes remain parallel. There is an "invariant line vector" (i.e., a special vector that does not expand, contract, or rotate) across the FCC and $L2_1$ lattices, as indicated by the white arrows in Fig. 3b. It is shown that the precipitation process of $Ni_2MnSn$ obeys the law of crystallographic representation theory of precipitation phase transition in the FCC/BCC system. The maximum close-packed plane mismatch, calculated from the average crystal plane spacing obtained in Fig. 3e is only 2.3%.

The inverse FFT patterns (Supplementary Fig. 8) reveal features of partially coherent interfaces. These low-mismatch semi-coherent interfaces have low driving force for migration[45], making it difficult for the $Ni_2MnSn$ precipitates to coarsen during the aging process, thus maintaining their sizes in the nanoscale. Besides the dimension constraint imposed by the interface, the geometric asymmetry of $Ni_2MnSn$ phases is achieved by anisotropic elastic strain field. As shown in Fig. 3a and f, the precipitates are evidently short along the $[1\bar{1}3]_{Cu}$. From the viewpoint of invariant line theory[46], the rapid growth direction of the orientation relationship between the phases under the condition of conforming to the invariant line can be obtained if the rotating

https://doi.org/10.1038/s41467-024-54904-9

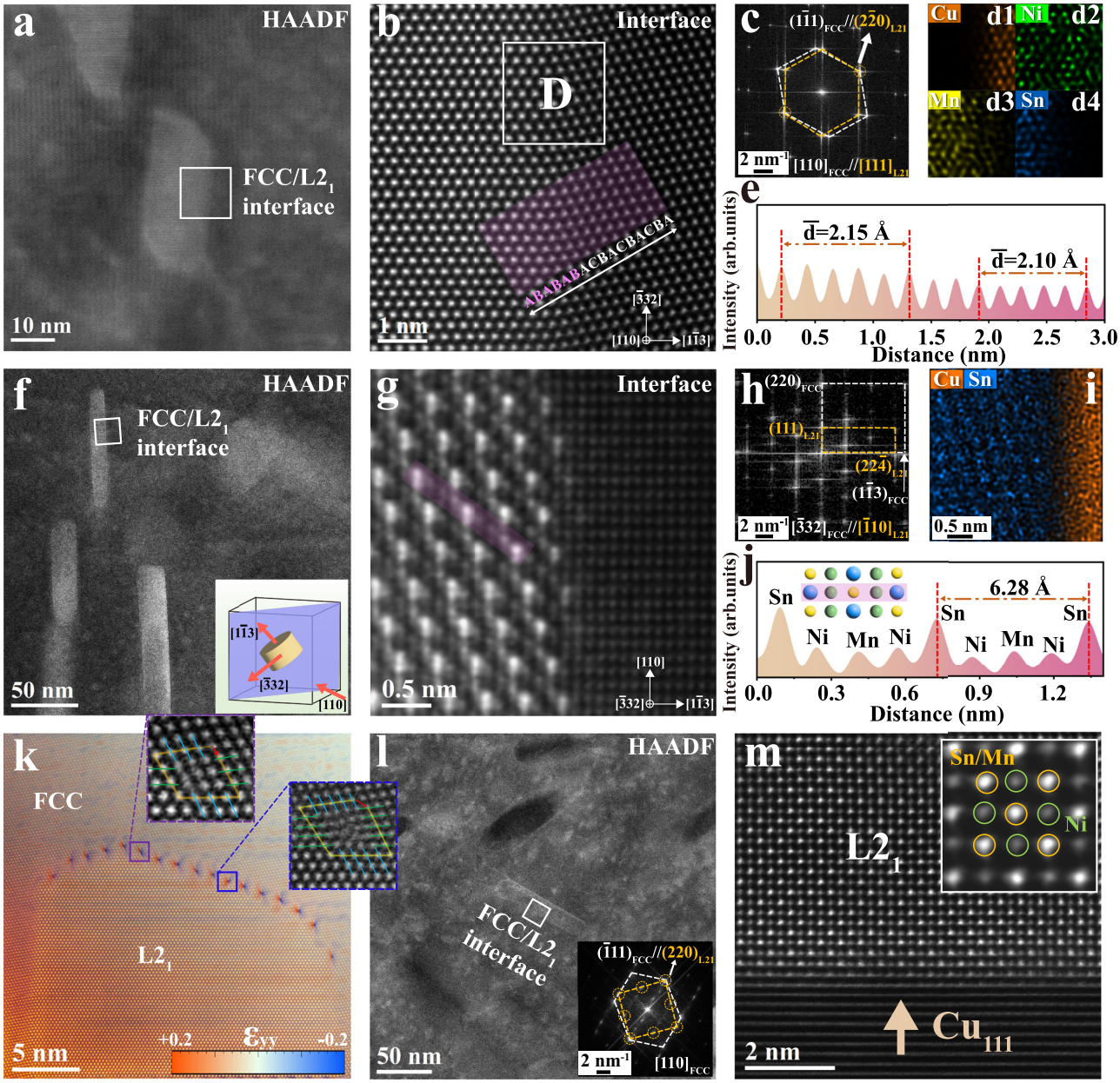


**Fig. 3 | Atomic-scale demonstration of the spatial configuration of the $Ni_2MnSn$ phase. a, f** The $Ni_2MnSn$ phase viewed along the $[110]_{Cu}$ and $[\bar{3}32]_{Cu}$ axes, respectively. The inset schematic diagram displays the three crystallographic axes of the matrix. **b, g** The corresponding $(1\bar{1}3)_{Cu}$/ $(112)_{Ni2MnSn}$ interface structures. **c, h** The corresponding Fast Fourier transform (FFT) patterns. **d1-d4, i** Corresponding atomic-scale EDX results. **e, j** Atomic intensity diagrams and interplanar spacing measurements in the transparent pink regions in (**b**) and (**g**). **k** A HAADF image showing the interface between FCC and $L2_1$ along the easy growth direction, superimposed with the GPA map ($\varepsilon_{yy}$). A zero-strain standard is set at the bottom-left corner. Purple and blue regions are zoomed in for Burgers circuit analysis. **l** Another form of the interface observed along the $[110]_{Cu}$ axes, identified by the corresponding FFT inset in the top-right corner. **m** The (111) Cu/ (220) $Ni_2MnSn$ interface and the atomic column morphology along the $[001]_{Ni2MnSn}$ axes.

conjugate plane and the principal strain (2.3%) are determined. The degree of elastic anisotropy can be quantified by the defined atomic effective spacing mismatch |δ | (see Methods for mismatch anisotropy calculations). The atomic effective spacing mismatch for the habit planes of Cu/$Ni_2MnSn$ is small (< 3%) along the two perpendicular in-plane vectors ($[\bar{3}32]_{Cu}$// $[\bar{1}10]_{Ni2MnSn}$ and $[110]_{Cu}$// $[111]_{Ni2MnSn}$), but relatively large (> 10%) along the out-of-plane vector. The mismatch anisotropy leads to a kinetic sluggishness of thickening of the $Ni_2MnSn$ precipitates in the $[1\bar{1}3]_{Cu}$ direction and relatively rapid growth along the lower elastic strain direction.

The growth behavior of the precipitates was further investigated by analyzing the interfaces along the rapid growth direction using STEM and geometric phase analysis (GPA) (Fig. 3k). Unlike the flat slow-growth $\{113\}_{Cu}$/ $\{112\}_{Ni2MnSn}$ interfaces, they exhibit zigzag arrays of interface dislocations. Internal stresses are mainly concentrated in these regions, which stabilize the FCC/$L2_1$ interface[47]. Analyses by Burgers circuit method show that the predominant dislocation configurations include the $\frac{a}{2}\langle 1\bar{1}2\rangle_{Cu}$ dislocation (purple region) and Hirth dislocation loops consisting of two different complete dislocations on $\{111\}_{Cu}$ planes (blue region). The establishment of low-index nanoledges through dislocation reactions reduces the overall interfacial energy[48] and compensates for residual mismatch strains with the matrix. This achieves an optimal balance between increased

elastic strain energy due to lateral expansion and reduced interfacial energy resulting from the introduction of periodic ledges.

An interface structure different from Fig. 3a was observed along the [110] $_{Cu}$ (Fig. 3l). The FFT illustration identifies a remarkable characteristic that the [100] $_{Ni2MnSn}$ zone axis goes through the center of the square ordered $L2_1$ spots. Conjugate spots of Cu (111111) and $Ni_2MnSn$ (220) coincide with each other, forming easily grown planes. The locally magnified image (Fig. 3m) shows an alternating distribution of bright Mn-Sn columns and dark Ni columns (Details are shown in Supplementary Fig. 9). Similar structures captured by HRTEM (Supplementary Fig. 10) may represent the intermediate states of precipitates, metastable phase, or other variants with K-S crystallographic orientation relationship.

### Mechanical properties

Figure 4a shows the engineering stress-strain curves of CA1, CA2 and CA3 at room temperature (see Supplementary Fig. 11 and Supplementary Table 5 for detailed aging hardening curves and summaries of mechanical properties). The mid-alloying CA2 (red curve) exhibits an exceptional combination of ultra-high strength and good ductility. The yield strength is 1129 MPa, with an ultimate tensile strength of around 1207 MPa and an elongation of 8.6%. In Fig. 4a, the low-alloying CA1 and the high-alloying CA3, as the contrast samples, are used to explore the performance range of Cu-Ni-Mn-Sn alloy.

The CA1 exhibits a yield strength of approximately 754 MPa and an ultimate tensile strength of around 836 MPa, accompanied by an elongation of 12.4%. The work hardening rate curve (Supplementary Fig. 12) confirms that CA1 maintains a stable strain hardening rate during plastic deformation. The CA3, has a yield strength of approximately 1506 MPa, which is nearly twice that of CA1, reflecting the strengthening upper limit of $Ni_2MnSn$. However, compared with CA1 and CA2, its work hardening ability drops sharply, which is related to the grain boundary embrittlement and strain inhomogeneity caused by local competitive coarsening of the $Ni_2MnSn$ precipitates. This has been confirmed by the corresponding fracture morphology (Supplementary Fig. 13) and microstructure (Supplementary Fig. 14). The fracture morphologies of CA1 and CA2 (Fig. 4a inset and Supplementary Fig. 13(d-i)) show fine dimples, indicating typical ductile fracture, while CA3 shows brittle cleavage fracture (Supplementary Fig. 13(a-c)). It is worth noting that the Cu-Ni-Mn-Sn alloys sit at the upper limit of the comparison diagram (Fig. 4b) among the currently reported high-strength Cu-based alloy (Supplementary Table 6).

The nanoprecipitate-dislocation interaction in CA2 after 8% strain was characterized by TEM, in order to reveal the strengthening and toughening mechanisms of Cu-Ni-Mn-Sn alloys. Figure 4c shows that dislocations are pinned at the interface of Cu/$Ni_2MnSn$ and bow out between the adjacent phases. The refined nanoparticles increase

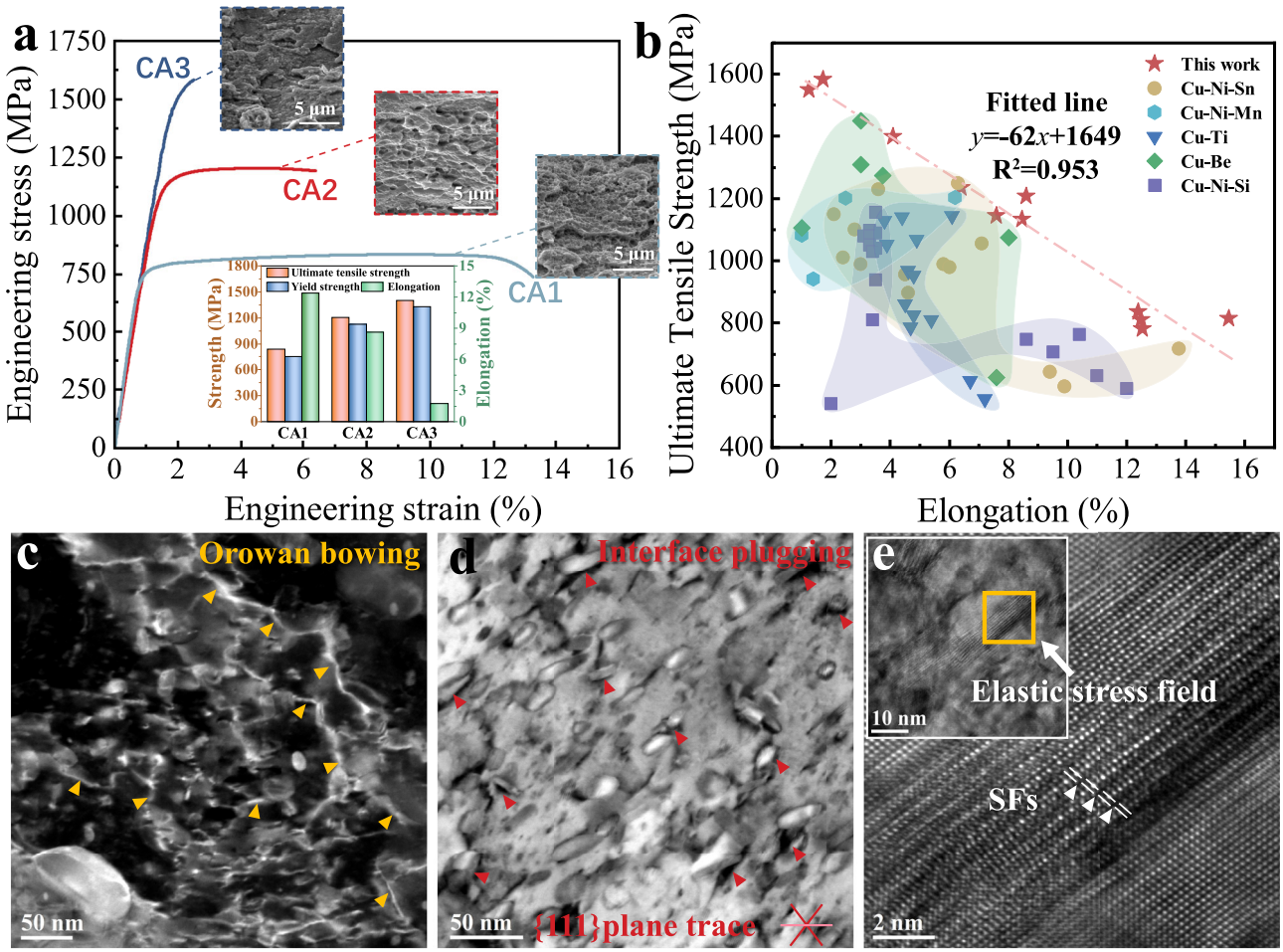


**Fig. 4 | Mechanical behavior and micro-strengthening mechanism of the Cu-Ni-Mn-Sn alloys. a** Engineering stress-strain curves, tensile fracture morphology and summary of ultimate tensile strength, yield strength and elongation for peak aged CA1, CA2 and CA3 at room temperature. **b** Comparison of ultimate tensile strength and elongation with other ultra-high strength copper alloys. **c, d** Nanoprecipitate-dislocation configuration after 8% plastic deformation, with gold triangles marking Orowan bowing, red triangles marking interface plugging of dislocations and red lines representing the {111} plane of the matrix. **e** HRTEM image of Ni-Mn-Sn phase co-deformed with matrix. Source data are provided as a Source Data file.

the total interface area, restricting the motion of dislocations within high-density nanoarrays and forming dislocation pile-up groups. Furthermore, due to the strong bonding at the $Ni_2MnSn$/Cu semi-coherent interface and the high aspect ratio of precipitates triggered by the mismatch anisotropic effect, dislocation glide along the {111} primary slip planes must overcome longer interfacial lattice resistance, as shown in Fig. 4d. Meanwhile, the strong $Ni_2MnSn$/Cu semi-coherent interface facilitates dynamic strain/stress distribution during loading[49], reducing the likelihood of strain localization due to lattice/elastic modulus mismatch and thus enhancing the co-deformation capability of the material because strain localization can lead to crack nucleation. Figure 4e shows that some stacking faults exist on the side of the dislocation pile-up, indicating that local stresses are relieved through stacking fault reactions near the interface to accommodate the co-deformation of the precipitates and the matrix. These features enhance the storage capacity of dislocations and shorten the average free path of dislocation motion[24], resulting in an effective combination of strain hardening and Orowan strengthening.

There are multiple strengthening mechanisms taking effect in the Cu-Ni-Mn-Sn system. In addition to the strong pinning effect of $Ni_2MnSn$ nanoprecipitates, they also include deformation-induced high-density dislocations[50–52], the solute drag effect of atomic scale heterogeneity[36,53,54], and lattice dislocation obstruction caused by micron-scale grain boundaries[55,56]. To quantify the strengthening capability of different mechanisms, we estimated the contributions of solid solution $\Delta\sigma_S$, dislocation substructure $\Delta\sigma_D$, precipitation strengthening $\Delta\sigma_P$, and grain boundary strengthening $\Delta\sigma_{GB}$ to the total yield strength $\sigma_{Total}$ by classical mechanical calculations (Supplementary Note. 1). For CA2, the values of $\Delta\sigma_P$, $\Delta\sigma_{GB}$, $\Delta\sigma_D$ and $\Delta\sigma_S$ are 716 MPa, 113 MPa, 198 MPa and 106 MPa respectively (Supplementary Table 8), giving $\sigma_{Total}$ of 1193 MPa, which is consistent with the experimental value of 1129 MPa. Among the different mechanisms, the strengthening contribution brought by the $Ni_2MnSn$ nanoprecipitates accounts for 60% of the total yield strength.

## Electromagnetic shielding performance

Figure 5a shows the frequency response curves of EMI-SE for CA1, CA2 and CA3 with a thickness of 2 mm in the range of 10 KHz-3 GHz. The average EMI-SE of CA2 reaches 110 dB in the whole test frequency band, which meets the performance target of the military shielding chamber ( ≥ 100 dB). In order to achieve a systematic understanding of the shielding mechanism of the Cu-Ni-Mn-Sn alloy, we analyzed the experimental results using the classical electromagnetic theory and established a multi-scale transmission matrix model[33,34] to explain the shielding mechanism below skin depth.

The experimental hysteresis loop(M-H) results show that all samples show soft magnetic characteristics (Fig. 5b). From CA1 to CA2 and then to CA3, the saturation magnetization Ms of the Cu-Ni-Mn-Sn alloys increased from 2.2 emu·g$^{-1}$ to 5.8 emu·g$^{-1}$, and then to 10.3 emu·g$^{-1}$ and the initial permeability ($\mu_i = \chi + 1$) increased from 1.25 to 1.82, and then to 2.54. This trend is largely due to the change in the structure parameters. Fig. 5d1-d3 show that the morphology of the particles in CA1, CA2 and CA3 gradually changes from near-spherical morphology (aspect ratio of 1:1 ~ 2:1) to anisotropic flaky morphology (aspect ratio of about 4:1 ~ 6:1), resulting in reduction of the demagnetization factor $N_d$. The fine and near-spherical precipitates in CA1 are likely due to the insufficient growth driving force of this low supersaturation alloy. When the radii of the precipitates become larger than the critical value, as likely in the cases of CA2 and CA3, the elastic strain energy can dominate the morphology and induce them to grow in the optimal direction[26]. Meanwhile, increasing the contents of the Ni, Mn and Sn alloying elements increases the volume fraction of $Ni_2MnSn$ ($V$). According to the Maxwell-Garnett mixing law[32]:

$$\mu_i = \frac{(\mu_{Ni_2MnSn} - 1)V}{(\mu_{Ni_2MnSn} - 1)(1 - V)N_d + 1} + 1 \quad (1)$$

the promotion of $\mu_i$ can be attributed to the increased number density and aspect ratio ($N_d$ decline) of the $Ni_2MnSn$ precipitates.

It should be pointed out that increasing the contents of the alloying elements also increases their contents in solid-solution simultaneously[52], which leads to a larger lattice distortion and raises the electron scattering probability (resistance rise). In other words, enhancement of the soft magnetic properties of the alloy is associated with declining of the electrical conductivity (Fig. 5a inset). Therefore, it is necessary to consider conductivity and permeability at the same time, in order to obtain a favorable shielding attenuation coefficient. The illustration in Fig. 5a shows that CA2 possesses the best combination of conductive and magnetic properties, i.e., the best EMI-SE. It is demonstrated that the shape anisotropy of precipitates and lattice distortion of the matrix of the Cu-Ni-Mn-Sn alloy can be controlled cooperatively by adjusting the contents of alloying elements, and an optimized electromagnetic loss performance can be realized.

We subsequently established a multi-scale electromagnetic numerical simulation model to quantitatively evaluate the main influence of the structure parameters of $Ni_2MnSn$ on frequency-shielding effectiveness response, based on the Maxwell equation, Drude model[57] and transmission matrix theory[34]. As shown in Fig. 5f, the attenuation process of electromagnetic waves in the alloy can be described as the product of the wave energy($E_0^+$, $E_0^-$) and repeated propagation matrix units with different thickness represented by Cu ($M_C$), $Ni_2MnSn$ ($M_N$), and their interfaces ($M_{(C,N)}$ or $M_{(N,C)}$). The propagation matrix for each unit was defined by the electromagnetic parameters, thickness ($d_{Cu}$ or $d_{Ni2MnSn}$), penetration angle($\theta_i$), and the frequency of the electromagnetic waves. The energy of the incident wave was attenuated to $E_{n+1}^+$ through absorption loss (SEA), reflection loss (SER), and multiple reflections in this process. The propagation characteristic matrix of the entire sample was subsequently used to calculate the EMI-SE (see Supplementary Note. 2 for details).

The simulation results are in good agreement with the experimental data of the Cu-Ni-Mn-Sn alloys in Fig. 5e. Separating different components of the EMI-SE data of the model shows that the ratio of SEA to SER is close to 6:4 (Fig. 5e inset). Given constant electromagnetic parameters, the parameter simulation results (Supplementary Fig. 15) show that, with the increase of the particle size and number density, SET and SEA increase, while SER changes little. It suggests that increasing particle size and number density is an effective method to prolong the path of electromagnetic wave penetrating the alloy, as high-density precipitates are beneficial to the formation of multiple alternating electrical and magnetic network structures[52,58]. The wave interacts with multiple nano-interfaces, resulting in additional attenuation of absorption[59] and leading to the improvement of SEA. In contrast, SER mainly depends on the wave impedance mismatch between the sample surface and free space, so it is not influenced much by the internal microstructure.

Figure 5e compares the Cu-Ni-Mn-Sn alloys with the existing metal-based structural EMSMs in EMI-SE and ultimate tensile strength. Their product of EMI-SE and ultimate tensile strength are above all the other structural EMSMs, underscoring the excellent comprehensive mechanical and electromagnetic shielding properties of the current alloy system. In addition, the Cu-Ni-Mn-Sn alloys show a higher Curie temperature ($T_C$) than bulk $Ni_2MnSn$ alloys (Fig. 5c). The high Tc is likely due to the chemical pressure effect[60] in Cu matrix or the change of valence electron concentration(e/a)[61] caused by antisite defects. This characteristic reveals their excellent anti-magnetization loss behavior at higher temperatures, which is beneficial to applications at elevated-temperatures.

https://doi.org/10.1038/s41467-024-54904-9

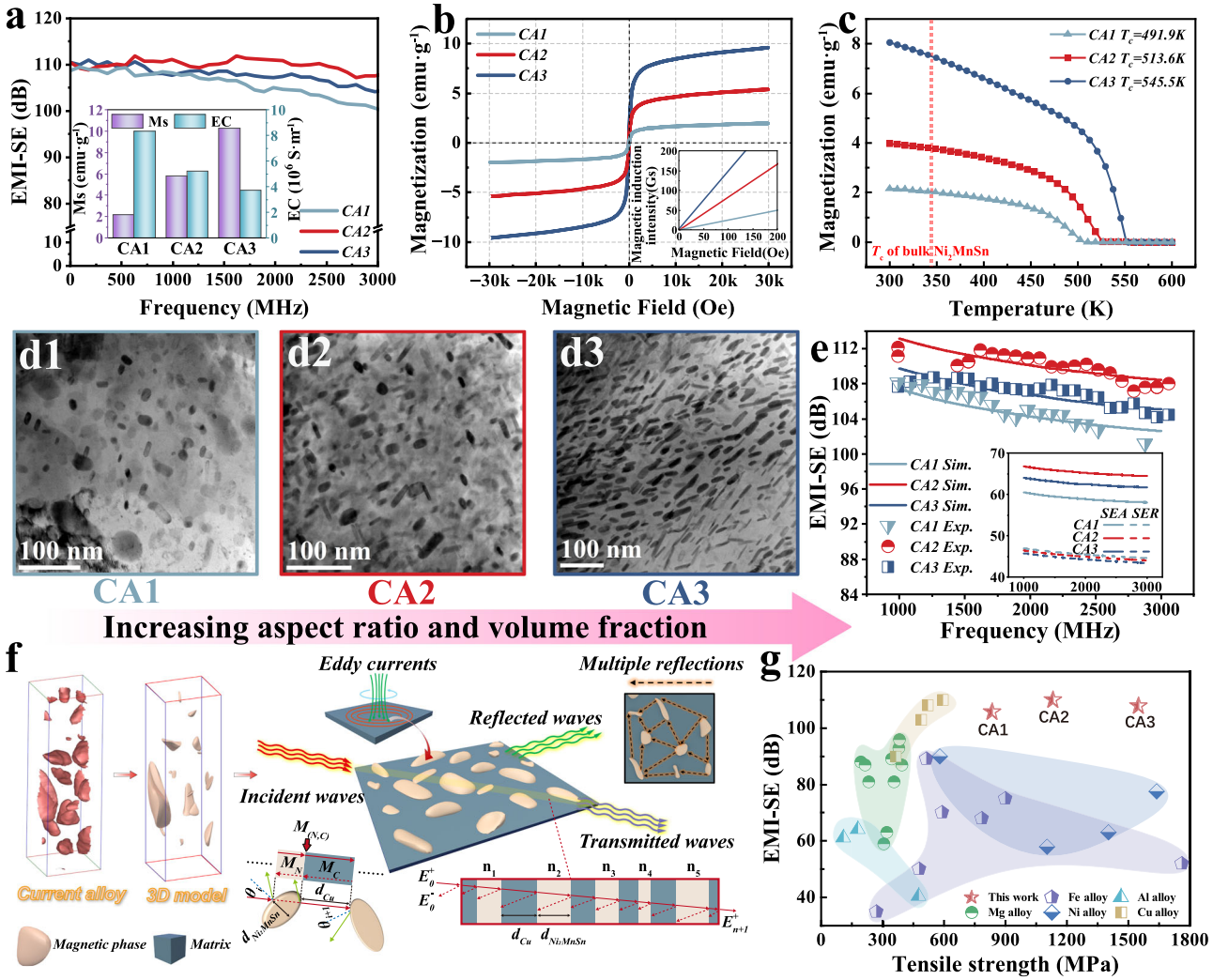


**Fig. 5 | Electromagnetic properties and electromagnetic shielding mechanism of the Cu-Ni-Mn-Sn alloys. a** EMI-SE values of the CA1, CA2 and CA3 samples with a thickness of 2 mm in the range of 10 kHZ-3000 MHz with the inset showing the saturation magnetization Ms (emu·g$^{-1}$) and electrical conductivity EC (S·m$^{-1}$) in the corresponding states. **b** Responses of Ms to varying applied magnetic field (M-H); **c** Responses of Ms to varying temperature(M-T). **d1-d3** Comparison of particle structure parameters of CA1, CA2 and CA3. **e** Comparison of EMI-SE between simulation and experimental results with the inset showing the calculated value of SEA and SER. **f** Electromagnetic shielding mechanism and schematic diagram of multi-scale transmission matrix model. **g** Comparison of EMI-SE (kHZ-GHz range and mm thickness) and ultimate tensile strength between previous metal-based EMSMs and current work. Detailed performance and literature are summarized in Supplementary Table 7. Source data are provided as a Source Data file.

To sum up, our work represents an effective method to achieve multi-objective properties of alloys through the design of precipitate structure parameters. By introducing the $Ni_2MnSn$ Heusler phase in Cu matrix and designing the nanoparticles with optimized structure parameters, ultra-high mechanical properties (yield strength = 0.71–1.50 GPa, ultimate tensile strength = 0.78–1.58 GPa) and excellent electromagnetic shielding effectiveness (100–110 dB at 10 kHz −3 GHz) are achieved. We show that the characteristics of low mismatch, high number density, small size, large aspect ratio, magnetic order and strong bonding of precipitates in the matrix are effective ways to realize a strong dislocation pinning effect and high-efficiency electromagnetic wave loss mechanism simultaneously. The approach of combining data-driven screening, multi-scale simulation and practical experiments is shown to be efficient and effective in developing precipitation-strengthened structural-functional alloys. It is worth noting that the current alloy system can be prepared by the traditional casting process, so it has great prospects for industrial applications.

## Methods

### Sample preparation

The Cu-9.85Ni-6.02Mn-5.05Sn alloy (CA2) was prepared by casting and subsequent thermomechanical treatment. The raw metallic materials were melted in a vacuum induction melting furnace in an argon atmosphere. The melt was poured into a graphite mold with a size of 130 mm × 130 mm × 100 mm and an 8 kg ingot was produced. The ingot was homogenized at 920 °C for 8 hours to eliminate dendrite segregation before cold-rolling by 50% (the 50% thickness reduction was completed in 6-7 passes, with each pass reducing by approximately 10%). Solid solution treatment was carried out at 850 °C for 1 hour to obtain a monophase structure. Multiple thermomechanical treatments (repeated 50% cold rolling and aging) were then carried out twice to obtain high-density $Ni_2MnSn$ precipitates. After 50% cold rolling for the third time, the samples with the final thickness of 2 mm were subjected to isothermal aging heat treatment at 300 °C–450 °C for different times (0 h, 8 h, 24 h, 48 h, 96 h, 128 h, 160 h) to explore the aging condition for the best particle size distribution. (Supplementary Fig. 1).

### Mechanical properties test

The micro-Vickers hardness was measured on an HV-5 low-load Vickers hardness tester, with a load of 3 kg and loading time of 10 s. A dog-bone tensile-test sample with a thickness of 1 mm, a width of 5 mm and a parallel section length of 30 mm was cut along the rolling direction by WEDM. The tensile test was conducted at room temperature on an INSTRON 1346 hydraulic universal testing machine, with a strain rate of $1 \times 10^{-3}$ $s^{-1}$.

### Electromagnetic performance test

The resistance values of the samples were measured by a QJ36s DC resistance tester using cuboid specimens with a dimension of 50 mm × 3 mm × 1 mm (length × width × thickness). The average value of three measurements was used to calculate the conductivity.

The hysteresis loop (M-H) test and the Curie temperature test (M-T) were performed by SQUID-VSM (MPMS-3). Cubic specimens of dimensions 2 mm × 2 mm × 2 mm were used for the measurements. The M-H was tested at room temperature in the magnetic field range of ±3 T, and the M-T was tested at 300K–600 K in a magnetic field set to 0.1 T.

The sample for the EMI-SE test has length and width of 20 mm, and thickness of 2 mm. EMI-SE was measured by a DR-S04 micro-coaxial shielding effectiveness testing device, with the scanning frequency ranging from 10 kHz to 3 GHz.

### Microscopic characterization

TEM analyses were conducted on the peak-aged samples. Discs with a diameter of 3 mm and a thickness of 0.3 mm were cut from the samples by WEDM. They were ground with 800, 1200 and 1600 mesh SiC sandpapers in sequence and then polished with a diamond solution. A Gatan 695 ion thinning instrument, with an ion beam energy of 5 KeV and an ion gun angle of ±8°, was used to thin the discs. The nano-to-atomic phase structure was characterized by an FEL Talos F200X transmission electron microscope.

The STEM-HAADF specimen was prepared by a SEM microscope equipped with a Ga focused-ion beam (FIB, 30 kV, Thermo Scientific Scios 2). In-situ sampling method was not used because the precipitates were evenly dispersed. The polished specimen was fixed, the front and back sides were hollowed out at random positions, and the remaining areas were U-cut. The thin sheet was taken out via Easylift and welded to a sample column on a copper net. Ion beam currents of 0.5 nA, 0.3 nA, 0.1 nA and 10 pA were used in sequence to further mill the piece into electron-transparent slices with a thickness of 70 nm. STEM-HAADF atomic images were captured by a Spectra300 double spherical aberration electron microscope at an accelerated voltage of 300 KV. Combined with the Super X energy spectrum module, the atomic-scale EDX analysis was carried out. GPA analysis[62] was based on the FFT of the STEM-HAADF atomic images, focusing a small aperture around a strong reflection, and performing IFFT. The phase component of the obtained complex images gave the local displacement information of the atomic plane, and the local strain component was obtained through calculation. QSTEM[44] image simulation was carried out by adopting a relaxed supercell, based on a multi-layer slicing algorithm, and the frozen phonon approximation method was used for analysis.

The atom probe tomography (APT) measurements were conducted by a local electrode atom probe (LEAP 5000XR) under UV laser pulsing at a pulse energy of 40 pJ, a pulse repetition rate of 200 kHz and a target evaporation rate of 0.5% per pulse at 50 K. The APT tip was also prepared by Ga-FIB milling. 3D reconstruction and component analysis of the APT data were conducted by CAMECA visualization and the analysis software AP Suite 6.3.0.90.

### First-principles calculation of enthalpy of formation and magnetic moment

The phase stability and effective magnetic moment calculations were carried out using the VASP[63] software package. The interaction potential between ions and valence electrons was described by the projected augmented wave (PAW) method[64,65]. The exchange correlation function was described by the generalized gradient approximation proposed by Predew, Burke, and Ernzerhof (GGA-PBE)[66]. The electron wave function was expanded in reciprocal space via the plane wave basis vector group. For calculating the bulk properties of FCC-Cu, the cut-off energy was set to 500 eV and the k-point was taken as the 11 × 11 × 11 Monkhorst-Pack grid. For calculating the bulk properties and magnetic moment of the $L2_1$ structure, the collinear spin polarization effect was considered. The plane wave cut-off energy was set to 500 eV, and the k-point was a 7 × 7 × 7 Monkhorst-Pack grid. The energy convergence value was less than $1 \times 10^{-5}$ eV/atom. The Hellmann-Feymann net force convergence standard of each atom was set to 0.01 eV/Å. After relaxation, the lattice parameters, static energy, total magnetic moment $M_{Tol}$, and local magnetic moment $M_{Mn}$ of Mn were obtained. The formation enthalpy of each atom of all candidates was calculated based on the following formula[45]:

$$\Delta H^{\text{diluteCu}} = \frac{(E_{Ni_{16}Mn_8X_8} - 16E_{Ni} - 8E_{Mn} - 8E_X^{\text{dilute Cu}})}{32} \quad (2)$$

where $E_{Ni_{16}Mn_8X_8}$, $E_{Ni}$ and $E_{Mn}$ are the static energies of $Ni_2MnX$ phase, the Ni element and the Mn element in the most stable state, respectively. $E_X^{\text{dilute Cu}}$ is the chemical potential of the X element in a dilute FCC Cu matrix. The lower the enthalpy of formation, the more stable the compound formed.

### Prediction matching interface via d-value mismatch

The modified Bramfitt formula[39] which is suitable for heterogeneous systems with FCC-BCC crystal structures, was used to calculate the d-value mismatch of the closest or near-closest pack planes: $\frac{2\left(d^{i_1j_1k_1}_{Ni_2MnX} - d^{i_2j_2k_2}_{Cu}\right)}{\left(d^{i_1j_1k_1}_{Ni_2MnX} + d^{i_2j_2k_2}_{Cu}\right)}$, where $d^{i_1j_1k_1}_{Ni_2MnX}$ and $d^{i_2j_2k_2}_{Cu}$ are the interplanar spacing of $Ni_2MnX$ and Cu, respectively. Only one possibility was found: the Cu (111) plane matches the $Ni_2MnX$ (220) plane, i.e., the closest pack planes of the two phases were parallel to each other (Supplementary Table 4). This finding is consistent with typical characteristics of most FCC-BCC systems[24]. In this matching mode, the d-value mismatch of almost all X elements was found to be in the range of 2%–2.3%, except for $Ni_2MnSi$, which is 3.9%.

### Prediction of morphology via mismatch strain anisotropy

Previous investigations[67,68] have shown that the influence of modulus inhomogeneity on the morphology of precipitates is not significant, even if the ratio of the elastic modulus of precipitate to matrix is large. For simplicity, we thus ignored the difference in elastic modulus and mainly considered the influence of mismatch strain anisotropy. In addition, we considered the phase interface mismatch anisotropy in the most stable Kurdjumov-Sachs(K-S) configuration, according to the common orientation relationship in the FCC-$L2_1$(BCC) system. It should be noted that although the combination of the closest pack planes of Cu and $Ni_2MnX$ under the K-S relationship is atomically flat[69], the closest pack plane here is not necessarily equivalent to the habitual plane. Therefore, we used the edge-to-edge model[41] to determine the "most favorable" region for atomic matching. This region satisfies a set of linear atomic rows and sawtooth atomic rows matching each other (directions a and b in Fig. 1b2). The c direction was obtained by the cross product of the a and b vectors. A constrained elastic mismatch parameter |δ|, which is defined as the relative difference of effective atomic spacing between precipitate and matrix lattice along a, b and c directions, was obtained from the density functional theory calculation. The interface matching region of two phases satisfying the K-S

relationship was obtained from the edge-to-edge model. The effective atomic spacing $a_{Ni_{16}Mn_8X_8}$, $a_{Cu}$, $b_{Ni_{16}Mn_8X_8}$, $b_{Cu}$, $c_{Ni_{16}Mn_8X_8}$, $c_{Cu}$ in three vertical directions of a, b, and c was measured by the VESTA[70] software. $|\delta|$ in a direction was calculated by $|\delta_a| = |\frac{a_{Ni_{16}Mn_8X_8} - a_{Cu}}{a_{Ni_{16}Mn_8X_8}}|$, and the same method applies to b and c directions.

## Data availability

All data generated or analyzed during this study are included in this published article (and its supplementary information files). All raw data in table format are available at https://doi.org/10.6084/m9.figshare.27246936. Source data are provided with this paper.

## References


1. Li, C. et al. Construction of polydopamine functionalized porous carbon network structure in polymer composites for excellent mechanical and electromagnetic interference shielding properties. *Carbon* **217**, 118620 (2024).
2. Wan, S. et al. High-strength scalable MXene films through bridging-induced densification. *Science* **374**, 96–99 (2021).
3. Zhou, Y. Material Foundation for Future 5 G Technology. *Acc. Mater. Res.* **2**, 306–310 (2021).
4. Cai, B. et al. Interface-induced dual-pinning mechanism enhances low-frequency electromagnetic wave loss. *Nat. Commun.* **15**, 3299 (2024).
5. Zhang Y. L., Gu J. W. A Perspective for Developing Polymer-Based Electromagnetic Interference Shielding Composites. *Nano-Micro Letters* **14**, 89 (2022).
6. Lv, H. et al. Staggered circular nanoporous graphene converts electromagnetic waves into electricity. *Nat. Commun.* **14**, 1982 (2023).
7. Lv, H. et al. A flexible electromagnetic wave-electricity harvester. *Nat. Commun.* **12**, 834 (2021).
8. Tang, Z. et al. Synthesis of CuCo2S4@Expanded Graphite with crystal/amorphous heterointerface and defects for electromagnetic wave absorption. *Nat. Commun.* **14**, 5951 (2023).
9. Fang, F., Li, Y.-Q., Xiao, H.-M., Hu, N. & Fu, S.-Y. Layer-structured silver nanowire/polyaniline composite film as a high performance X-band EMI shielding material. *J. Mater. Chem. C.* **4**, 4193–4203 (2016).
10. Lei, X. et al. Investigation of electrical conductivity and electromagnetic interference shielding performance of Au@CNT/sodium alginate/polydimethylsiloxane flexible composite. *Compos. Part A: Appl. Sci. Manuf.* **130**, 105762 (2020).
11. Deng, Z., Tang, P., Wu, X. & Zhang, H.-B. Yu Z-Z. Superelastic, Ultralight, and Conductive Ti3C2Tx MXene/Acidified Carbon Nanotube Anisotropic Aerogels for Electromagnetic Interference Shielding. *ACS Appl. Mater. Interfaces* **13**, 20539–20547 (2021).
12. Pavlou, C. et al. Effective EMI shielding behaviour of thin graphene/PMMA nanolaminates in the THz range. *Nat. Commun.* **12**, 4655 (2021).
13. Sun, Y. et al. A facile synthesis of FeNi3@C nanowires for electromagnetic wave absorber. *J. Alloy. Compd.* **586**, 688–692 (2014).
14. Liu, X. et al. Graphene-enhanced microwave absorption properties of Fe3O4/SiO2 nanorods. *Compos. Part A: Appl. Sci. Manuf.* **89**, 40–46 (2016).
15. Zhao, R. et al. Highly anisotropic Fe3C microflakes constructed by solid-state phase transformation for efficient microwave absorption. *Nat. Commun.* **15**, 1497 (2024).
16. He, M. et al. Shape Anisotropic Chain-Like CoNi/Polydimethylsiloxane Composite Films with Excellent Low-Frequency Microwave Absorption and High Thermal Conductivity. Preprint at https://doi.org/10.1002/adfm.202316691 (2024).
17. Arzt, E. Size effects in materials due to microstructural and dimensional constraints: a comparative review. *Acta Materialia* **46**, 5611–5626 (1998).
18. Krenke, T. et al. Inverse magnetocaloric effect in ferromagnetic Ni–Mn–Sn alloys. *Nat. Mater.* **4**, 450–454 (2005).
19. Kamarád, J. et al. Magnetization and exchange-bias effect in powders of the Heusler Ni2MnSn-based alloys. *J. Alloy. Compd.* **976**, 173157 (2024).
20. Yang, J. et al. Manipulation of thermal hysteresis and magnetocaloric effect in the Ni-Co-Mn-In alloys through lattice contraction: Effect of Ge substitution for In. *Acta Materialia* **246**, 118694 (2023).
21. Feng, J. et al. Significant high-frequency electromagnetic wave absorption performance of Ni2 + xMn1−xGa alloys. *J. Mater. Sci.* **53**, 11779–11790 (2018).
22. Dubiel, Ł., Stefaniuk, I., Wal, A. & Kuźma, M. Effect of annealing on the magnetic ordering and electron magnetic resonance of melt-spun Ni-Mn-In ribbons. *J. Magn. Magn. Mater.* **504**, 166638 (2020).
23. Meng, J., Xie, L., Yu, Q., Wang, J. & Jiang, C. Toughening the grain boundaries by introducing a small amount of the second phase: Ni-Cu-Mn-Ga shape memory alloys as an example. *Acta Materialia* **263**, 119469 (2024).
24. Jang, T. J. et al. Shear band-driven precipitate dispersion for ultrastrong ductile medium-entropy alloys. *Nat. Commun.* **12**, 4703 (2021).
25. Millán, J. et al. Designing Heusler nanoprecipitates by elastic misfit stabilization in Fe–Mn maraging steels. *Acta Materialia* **76**, 94–105 (2014).
26. Kim, W. C. et al. Designing L21-strengthened Al-Cr-Fe-Ni-Ti complex concentrated alloys for high temperature applications. *Acta Materialia* **211**, 116890 (2021).
27. Han, L. et al. A mechanically strong and ductile soft magnet with extremely low coercivity. *Nature* **608**, 310–316 (2022).
28. Han, L. et al. Strong and ductile high temperature soft magnets through Widmanstätten precipitates. *Nat. Commun.* **14**, 8176 (2023).
29. Wang, L., Lu, W., Hu, Q., Xia, M. & Wang, Y. Li J-g. Interfacial tuning for the nucleation of liquid AlCu alloy. *Acta Materialia* **139**, 75–85 (2017).
30. Jiang, S. et al. Ultrastrong steel via minimal lattice misfit and high-density nanoprecipitation. *Nature* **544**, 460–464 (2017).
31. Peng, B. et al. Machine learning-enabled constrained multi-objective design of architected materials. *Nat. Commun.* **14**, 6630 (2023).
32. Rozanov, K. N., Li, Z. W., Chen, L. F. & Koledintseva, M. Y. Microwave permeability of Co2Z composites. *J. Appl. Phys.* **97**, 013905 (2004).
33. Yun, T. et al. Electromagnetic Shielding of Monolayer MXene Assemblies. *Adv. Mater.* **32**, 1906769 (2020).
34. Wu, C. et al. A multi-scale model to predict the electromagetic interference shielding performance of (Fe/Cu)@CNT/SA/PDMS flexible composite. *J. Alloy. Compd.* **927**, 167043 (2022).
35. Graf, T., Felser, C. & Parkin, S. S. P. Simple rules for the understanding of Heusler compounds. *Prog. Solid State Chem.* **39**, 1–50 (2011).
36. Wang, Y. et al. Synthesis of High-Entropy-Alloy Nanoparticles by a Step-Alloying Strategy as a Superior Multifunctional Electrocatalyst. *Adv. Mater.* **35**, 2302499 (2023).
37. Zhang, Y., Zhou, Y. J., Lin, J. P., Chen, G. L. & Liaw, P. K. Solid-Solution Phase Formation Rules for Multi-component Alloys. *Adv. Eng. Mater.* **10**, 534–538 (2008).
38. Wu, G. et al. Elemental partitioning-mediated crystalline-to-amorphous phase transformation under quasi-static deformation. *Nat. Commun.* **15**, 1223 (2024).

39. Bramfitt, B. L. The effect of carbide and nitride additions on the heterogeneous nucleation behavior of liquid iron. *Metall. Trans.* **1**, 1987–1995 (1970).
40. Ji, J. et al. Zinc-Contained Alloy as a Robustly Adhered Interfacial Lattice Locking Layer for Planar and Stable Zinc Electrodeposition. *Adv. Mater.* **35**, 2211961 (2023).
41. Zhang, M. X. & Kelly, P. M. Edge-to-edge matching model for predicting orientation relationships and habit planes—the improvements. *Scr. Materialia* **52**, 963–968 (2005).
42. Stearns MBJJoAP. Hyperfine field and magnetic behavior of Heusler alloys. **50**, 2060-2062 (1979).
43. Moya, X. et al. Martensitic transition and magnetic properties in Ni–Mn–X alloys. *Mater. Sci. Eng.: A* **438-440**, 911–915 (2006).
44. Koch C. T. Determination of core structure periodicity and point defect density along dislocations. Arizona State University (2002).
45. Chung, H. et al. Doubled strength and ductility via maraging effect and dynamic precipitate transformation in ultrastrong medium-entropy alloy. *Nat. Commun.* **14**, 145 (2023).
46. Yi, J. et al. Precipitation behavior of Cu-3.0Ni-0.72Si alloy. *Acta Materialia* **166**, 261–270 (2019).
47. Li, Z. et al. Strength, plasticity and coercivity tradeoff in soft magnetic high-entropy alloys by multiple coherent interfaces. *Acta Materialia* **254**, 118970 (2023).
48. Zhang, Z., Rosalie, J. M., Medhekar, N. V. & Bourgeois, L. Resolving the FCC/HCP interfaces of the γ′ (Ag2Al) precipitate phase in aluminium. *Acta Materialia* **174**, 116–130 (2019).
49. Chen, X. et al. Regulating microstructure of Al matrix composites with nanocarbon architecture design towards prominent strength-ductility combination. *Scr. Materialia* **222**, 115037 (2023).
50. Cai, H. et al. Synergistic effects of trace silicon, calcium and cerium on the microstructure and properties of a novel Cu–Cr–Nb–Si–Ca–Ce alloy. *Mater. Sci. Eng.: A* **898**, 146419 (2024).
51. Li, X. et al. Microstructure and properties of high strength, high conductivity Cu-2.5Fe-0.3Cr-0.3Mg-0.2Si-0.1Ca-0.1Zr alloy treated by multi-stage thermomechanical treatment. *Mater. Charact.* **207**, 113601 (2024).
52. Lv, X. et al. Effects of Si addition on mechanical, electrical and magnetic property of Cu-10Fe alloy. *Mater. Charact.* **196**, 112612 (2023).
53. Cao, X. et al. FeNiCrCoMn High-Entropy Alloy Nanoparticles Loaded on Carbon Nanotubes as Bifunctional Oxygen Catalysts for Rechargeable Zinc-Air Batteries. *ACS Appl. Mater. Interfaces* **15**, 32365–32375 (2023).
54. Jiang, Z. et al. A low-density polymer/CrMnFeCoNi composite with high strength and high damping capacity. *Compos. Part A: Appl. Sci. Manuf.* **181**, 108130 (2024).
55. Xia, Z. et al. Effect of G-phase and heterogeneous deformation-induced strengthening on the mechanical properties of Cu-20Ni-20Mn-2Fe-1Si alloy. *Mater. Charact.* **205**, 113325 (2023).
56. Yu, X. et al. Effect of Mg content on the microstructure and properties of high strength, high conductivity Cu–Fe–Cr–Si–Mg alloy. *Mater. Sci. Eng.: A* **883**, 145510 (2023).
57. Hong, J. et al. Best practices for correlating electrical conductivity with broadband EMI shielding in binary filler-based conducting polymer composites. *Chem. Eng. J.* **455**, 140528 (2023).
58. Pang, Y. et al. Microstructure and properties of high strength, high conductivity and magnetic Cu–10Fe-0.4Si alloy. *Mater. Sci. Eng.: A* **826**, 142012 (2021).
59. Iqbal, A. et al. Anomalous absorption of electromagnetic waves by 2D transition metal carbonitride Ti3CNTx (MXene). *Science* **369**, 446–450 (2020).
60. Kamarád, J. et al. Pressure study of magnetism in off-stoichiometric Ni2MnSn-based alloys. *J. Magn. Magn. Mater.* **539**, 168345 (2021).
61. Krenke, T. et al. Martensitic transitions and the nature of ferromagnetism in the austenitic and martensitic states of Ni-Mn-Sn alloys. *Phys. Rev. B* **72**, 014412 (2005).
62. Hÿtch, M. J., Snoeck, E. & Kilaas, R. Quantitative measurement of displacement and strain fields from HREM micrographs. *Ultramicroscopy* **74**, 131–146 (1998).
63. Vanderbilt, D. Soft self-consistent pseudopotentials in a generalized eigenvalue formalism. *Phys. Rev. B* **41**, 7892–7895 (1990).
64. Blöchl, P. E. Projector augmented-wave method. *Phys. Rev. B* **50**, 17953–17979 (1994).
65. Kresse, G. & Joubert, D. From ultrasoft pseudopotentials to the projector augmented-wave method. *Phys. Rev. B* **59**, 1758–1775 (1999).
66. Perdew, J. P., Burke, K. & Ernzerhof, M. Generalized Gradient Approximation Made Simple. *Phys. Rev. Lett.* **77**, 3865–3868 (1996).
67. Wang, Y. et al. A combined simulation and experimental study of the equilibrium shapes of η′ and α precipitates in Mn-containing 7xxx Al-alloys. *Acta Materialia* **259**, 119094 (2023).
68. Yu, T. et al. H-phase precipitation and its effects on martensitic transformation in NiTi-Hf high-temperature shape memory alloys. *Acta Materialia* **208**, 116651 (2021).
69. Zhang, R. F., Wang, J., Beyerlein, I. J. & Germann, T. C. Dislocation nucleation mechanisms from fcc/bcc incoherent interfaces. *Scr. Materialia* **65**, 1022–1025 (2011).
70. Momma K. & Izumi FJJoAC. VESTA 3 for three-dimensional visualization of crystal, volumetric and morphology data. *J. Appl. Crystallogr.* **44**, 1272–1276 (2011).


## Acknowledgements

This work is supported by the National Natural Science Foundation of China (No. 92366202, No. 52271125), Science Fund for Distinguished Young Scholars in Hunan Province (No. 2024JJ2078), National Key R&D Program of China (No. 2021YFB3501003), High Performance Computing Center of Central South University.

## Author contributions

Z.X. guided the research project with S.G. and Z.L.; Z.X. and Z.J. conducted the alloys preparation; Z.X., X.H. and J.L. tested the properties and characterized the microstructure of the alloys; Z.X., W.D. and L.L. conducted the simulation; Z.X., S.G., Y.Z., and Z.L. conceptualized the paper. Z.X., Y.Z. and S.G. contributed to the writing of the paper. All authors participate in the discussion.

## Competing interests

The authors declare no competing interests.

## Additional information

**Supplementary information** The online version contains supplementary material available at https://doi.org/10.1038/s41467-024-54904-9.

**Correspondence** and requests for materials should be addressed to Shen Gong or Zhou Li.

**Peer review information** *Nature Communications* thanks Rastislav Varga and the other, anonymous, reviewer(s) for their contribution to the peer review of this work. A peer review file is available.